Received: 2 November 2023 | Revised: 29 December 2023 | Accepted: 25 January 2024

DOI: 10.1111/jace.19750

Journal of the American Ceramic Society

RESEARCH ARTICLE

High-strength Si–SiC lattices prepared by powder bed fusion, infiltration-pyrolysis, and reactive silicon infiltration

Marco Pelanconi[1,2] | **Samuele Bottacin**[1] | **Giovanni Bianchi**[1] | **Dietmar Koch**[3] | **Paolo Colombo**[2,4] | **Alberto Ortona**[1]

[1]University of Applied Sciences (SUPSI): Mechanical Engineering and Materials Technology Institute (MEMTi), Polo Universitario Lugano, Lugano, Switzerland

[2]Department of Industrial Engineering, University of Padua, Padua, Italy

[3]Institute of Materials Resource Management, University of Augsburg, Augsburg, Germany

[4]Department of Materials Science and Engineering, The Pennsylvania State University, University Park, Pennsylvania, USA

Correspondence
Marco Pelanconi, University of Applied Sciences (SUPSI): Mechanical Engineering and Materials Technology Institute (MEMTi), Polo Universitario Lugano, 6962 Lugano, Switzerland.
Email: marco.pelanconi@supsi.ch

Editor's Choice
The Editor-in-Chief recommends this outstanding article.

Abstract

This study focuses on the design, additive manufacturing, and characterization of silicon carbide-based components with complex geometries. These parts were produced using a novel hybrid technique, previously developed: powder bed fusion of polyamide was used to 3D print two different templates with complex architectures. Preceramic polymer infiltrations and pyrolysis with polycarbosilane and furan resin were performed to obtain the ceramic parts. The final densification was achieved with reactive or nonreactive silicon infiltrations according to four different strategies, producing ceramics comprised of crystalline βSiC, reaction-bonded βSiC, and low residual silicon. The final gyroid samples (~70 vol% macroporosity) exhibited a maximum compressive strength of 24.7 ± 2.2 MPa, with a skeleton density of 3.173 ± 0.022 g/cm^3, and a relative density of 0.935 ± 0.016. These findings underscore the potential of this manufacturing approach and showcase its effectiveness in fabricating intricate ceramic structures for engineering applications as heat exchangers and catalytic supports.

KEYWORDS
additive manufacturing, powder bed fusion, preceramic polymers, silicon carbide, silicon infiltration

1 | INTRODUCTION

The fabrication of silicon carbide (SiC) ceramic structures with intricate geometries is a cumbersome and expensive process when using standard techniques and machining. The development of additive manufacturing (AM) has revolutionized the fabrication of many materials including SiC.[1] This approach allows for the realization of complex architectures, including cellular structures,[2,3] which were previously unattainable through conventional manufacturing methods. One of the most significant challenges in AM of SiC ceramics is achieving complete densification and thus obtaining higher mechanical properties.[4–6] To address it, after green preform printing, subsequent infiltration methods have been employed, such as preceramic polymer infiltration and pyrolysis (PIP),[7,8] liquid silicon infiltration (LSI),[9,10] and chemical vapor infiltration.[11–13] These infiltration techniques help to increase the relative density, strength, and overall performance of the SiC ceramic parts.[14–17] The combination of AM and subsequent infiltration methods provides several advantages.[18] These include the ability to produce complex parts with

fine details, rapid prototyping, reduction of material waste, and the flexibility to customize components for specific applications. Nevertheless, several challenges remain to be addressed. One of the limitations of conventional AM methods, such as selective laser sintering or binder jetting, is the limited control over the ceramic microstructure resulting after manufacturing, which leads to insufficient density and poor mechanical properties.[19,20] The integration of AM with the powder bed fusion (PBF) of a polymeric preform, followed by preceramic PIP and LSI, has shown great promise for the fabrication of SiC and SiSiC parts.[21] Our previous work on this technique successfully demonstrated its feasibility in producing simple shapes like a disc.[22] However, the potential for manufacturing complex Si–SiC parts with intricate geometries was not yet explored.

In this article, we present the follow up of this novel technique to produce complex SiC-based parts, highlighting its capabilities and advantages over other AM methods. The utilization of the proposed technique opens up new possibilities for the production of complex SiC-based parts. By designing the polymeric preform and optimizing the PBF parameters, complex shapes with extremely fine details and controlled microstructure can be achieved. The subsequent PIP and LSI processes play a crucial role in transforming the polymeric preform into a fully dense SiC-based part. The PIP step allows for the infiltration of the preform with a ceramic precursor, which upon pyrolysis, converts into a ceramic matrix. This process not only enhances the density and mechanical properties of the part but also allows for the preservation of complex geometries and fine details.[23–26] The final LSI process further enhances the density and strength by infiltrating the pyrolyzed preform with liquid silicon, resulting in high-dense and net shape components.[27–33] The ability to fabricate complex SiC parts using this novel technique opens up a wide range of applications.[34,35] These include aerospace components with intricate cooling channels, biomedical implants with customized geometries, energy systems with complex internal flow paths, and catalytic supports.[36] The excellent mechanical properties, thermal stability, and chemical resistance of SiC make it an ideal material for demanding environments where performance and reliability are critical.[37] This advancement pushes the boundaries of SiC-based applications, enabling the realization of complex SiC parts in various industries.[38,39]

2 | MATERIALS AND METHODS

The newly developed hybrid technique[21,22,40] leverages a combination of 3D printing of polymer powders, precursor infiltration, pyrolysis, and LSI to produce complex ceramic 3D architectures. The process begins with the PBF technology to create a polyamide preform with high microporosity. This microporosity is crucial for achieving successful infiltration using a liquid preceramic polymer, leading to a more efficient conversion into ceramics. Subsequently, pyrolysis at a temperature of 1000°C is employed to produce the polymer-derived ceramic body, with the decomposition of the polyamide preform, and few PIP cycles with different precursors are performed to enhance the relative density of the part. The final densification is achieved though infiltration with molten silicon at 1800°C (The infiltration temperature was selected based on preliminary tests, as reported in the **Supporting Information**). In this work, four infiltration strategies (see Section 2.3) were investigated to produce dense Si–SiC and SiC–SiC parts with high mechanical strength (see Graphical Abstract).

2.1 | Computational design of the complex architectures

Two structures with high geometric complexity were generated through a parametric computational design approach in view of their fabrication via PBF. The 3D models were created using a tool developed into Grasshopper (McNeel), which allows to generate high complex cellular structures with different topologies. The unit cells of the strut-based rotated cube (RC) and the surface-based gyroid (GY) were modeled with a cell size of 2.9 and 6.8 mm, respectively. The minimal surface of the GY is described by the following equation:

$$\mathrm{GY} = \sin x \cdot \cos y + \sin y \cdot \cos z \cdot \sin z \cdot \cos x \quad (1)$$

The single unit cells were then replicated until forming the final cylindrical samples with 25 mm diameter and 44 mm height. The RC lattice consisted of struts with a diameter of 1.1 mm, whereas the GY structure consisted of surfaces with a thickness of 1.0 mm. The designs resulted in two structures with the same specific surface area of 947 m^{-1} (normalized on the occupied volume) and geometric macroporosity of 67 vol%. Figure 1 shows the two structures in different views.

2.2 | Manufacturing

2.2.1 | Materials

Spherical powders (d_{50} = 60 μm) of polyamide 12 (PA12, Sintratec AG) were used for the 3D printing. PA12 is a

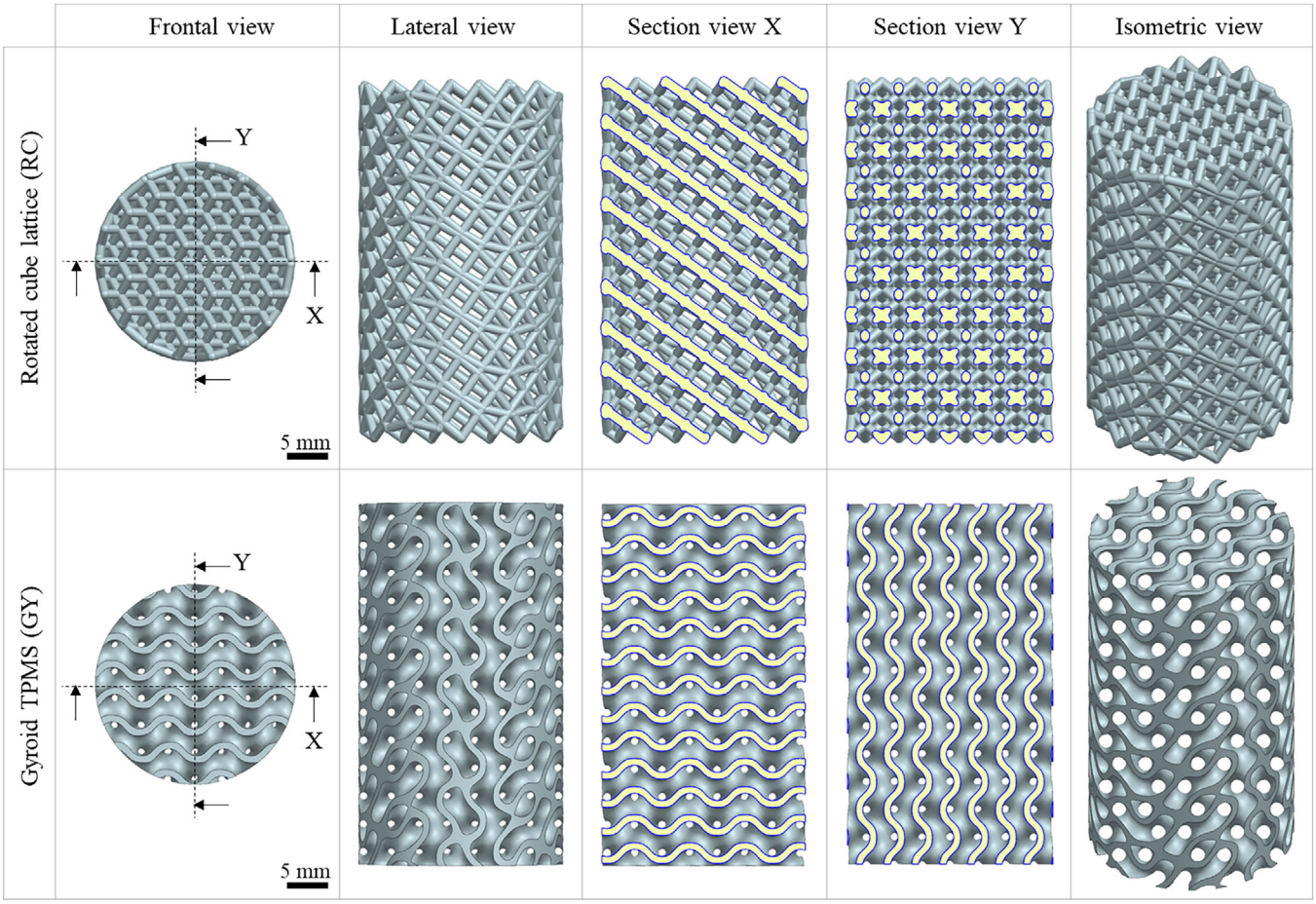

FIGURE 1 3D computational design models of the rotated cube and the gyroid structures investigated in this work.

thermoplastic and semicrystalline-crystalline polymer suitable for the PBF technique, with a density of 1.0 g/cm^3.

Two different liquid preceramic polymers were used for the infiltration of the 3D printed preforms: (i) allylhydridopolycarbosilane (AHPCS) polymer (StarPCS SMP-10, Starfire Systems Inc) and (ii) furanic (FUR) resin (Furolite 100, TransFurans Chemicals). Both preceramic polymers have about the same density of 1.0 g/cm^3 and dynamic viscosity of 40–100 cPs at 25°C. In the cases of FUR resin, the addition of a catalyst (HM 1448, WIZ chemicals) was needed to promote its crosslinking. In a previous work,[40] the authors found that the pyrolysis at 1000°C in inert atmosphere produces amorphous SiC from AHPCS and amorphous C from FUR with ceramic yield of 75% and 52%, respectively. Moreover, AHPCS pyrolysis at higher temperature forms βSiC with true density of 3.206 ± 0.099 g/cm^3.

Graphite ($C_{(g)}$) powder (d_{90} = 12.6 μm and d_{50} = 6.2 μm) (TIMREX KS 10, Imerys) was mixed (13% wt) with the AHPCS liquid polymer and used for the infiltration case #4 (see Section 2.2.3) with the aim to achieve the reaction between silicon and graphite to produce silicon carbide.

Silicon grains (HQ1, Sicerma) with a size of 0.2–2.0 mm were used to perform the LSI.

2.2.2 | 3D printing of the polymeric preform

The polymeric preforms were manufactured utilizing a Sintratec KIT, a commercial PBF 3D printer (Sintratec KIT, Sintratec AG). The printing process was performed in air involving three main phases. (i) Preprocessing: The 3D CAD model of the object was sliced into two-dimensional cross-sections, the printing parameters were defined and uploaded in the machine. The chamber and the powder bed were heated to reach and maintain a uniform temperature within the PA12 sintering window to minimize the energy required for the melting. (ii) Processing (see Figure 2): The build platform was lowered by a preset distance (layer thickness) and the delivery platform was uplifted. Then, the recoating blade deposited a new powder layer. Finally, the laser traced the component cross-section providing thermal energy to selectively melt the powders. (iii) After natural cooling of the chamber the 3D printed part was removed. The non-melted powder around and

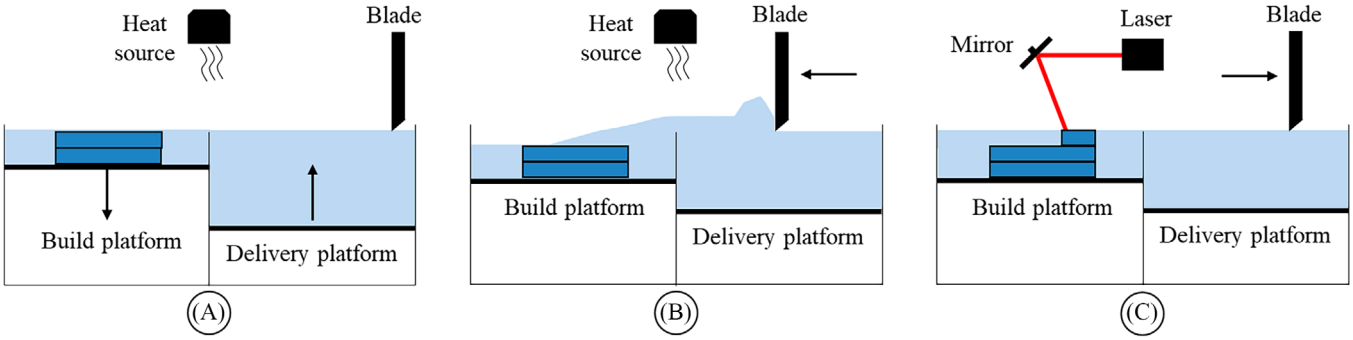

FIGURE 2 Schematic of the powder bed fusion (PBF) technology for polymeric powders: (A) lowering of the build platform by a fixed layer thickness and uplift of the delivery platform, meanwhile the chamber temperature is regulated by a heat source; (B) deposition of a new powder layer by the blade and heating of the new powder layer; (C) selectively melting of the polymer powders by the laser beam driven by motorized mirrors.

inside the part was carefully removed using compressed air. The following 3D printing parameters were used:

- Laser speed of 848 mm/s.
- Layer thickness of 100 μm.
- Powder surface temperature of 166°C.

This combination of parameters (previously optimized by the authors[22]) allows to 3D print parts with high microporosity and overall quality in terms of resolution and accuracy.

2.2.3 | Precursor infiltration and pyrolysis

A purpose-built apparatus was used to infiltrate the 3D-printed complex preforms with the selected liquid precursors, operating in light vacuum ($\sim 10^{-1}$ bar) and at room temperature. A planetary centrifugal mixer (Thinky Mixer ARE-250, Thinky) was used to mix the preceramic polymer with its catalyst at 700 rpm for 3 min. The FUR infiltrated samples were pre-cured in a static furnace at 145°C for 2 h. This was found to be a crucial step in promoting the crosslinking of the FUR resin and maintaining the shape of the part after pyrolysis. After each infiltration, the samples were subjected to heat treatment in a vertical retort furnace (SPS01, Keos Srl) using high purity flowing argon (99.99%, 30 L/h) at the temperature of 1000°C for 1 h (heating rate of 51°C/h). A detailed description of the thermal cycle is provided in our previous work.[22]

2.2.4 | High temperature pyrolysis (HTP)

Before LSI, all the samples were subjected to pyrolysis at 1800°C for 1 h in order to crystallize the ceramic matrix and to increase their microporosity, which has been found to be useful in achieving successful subsequent infiltration with molten silicon. A graphite resistor furnace (XGRAPHITE 2200, XERION GmbH) was used for carrying out the high temperature pyrolysis (HTP). During the process, the chamber was heated at 20°C/min, the absolute pressure was held at 5 mbar, and an argon flow rate of 1 L/min was imposed for safety reasons.

2.2.5 | Liquid silicon infiltration

The final densification was performed through LSI at 1800°C for 1 h at the same conditions of the HTP treatment. A silicon content of 120% with respect to the sample weight was used to infiltrate the materials. The reason for these conditions is reported in the **Supporting Information**, which shows the investigation of three parameters affecting the LSI process, namely, temperature, time, and silicon content.

Two types of LSI techniques were employed: (a) non-reactive silicon infiltration, which does not involve a chemical reaction between the molten silicon and the substrate material and (b) reactive silicon infiltration, also known as reactive melt infiltration, which involves the reaction between the molten silicon and the free carbon generated by the pyrolysis of a C precursor (or added graphite powder) to form a solid matrix of SiC, named reaction bonded SiC (RBSiC),[30,41] according to the following reaction:

$$\mathrm{Si}\,(l) + \mathrm{C}\,(s) \rightarrow \mathrm{SiC}\,(s) \quad [\,\Delta H_{1773\ \mathrm{K}} = -123\ \mathrm{kJ/mol}] \qquad (2)$$

where l is liquid, s is solid, and ΔH is the enthalpy of formation. Increasing the content of SiC with respect to the residual Si phase is of significant industrial interest

because of the benefits achievable in terms of density and mechanical strength.

2.3 | Summary of the infiltration strategies

Four different strategies were used to infiltrate the 3D printed preforms and to produce ceramic templates to be further infiltrated with molten silicon at higher temperature. The aim was to find the best strategy to produce dense and strong SiC-based ceramics. The strategies are listed below:

1. Five PIP cycles were performed with AHPCS to obtain a high degree of densification of the amorphous SiC matrix. Then, HTP was performed to achieve the crystallization of the SiC into βSiC. The final densification was performed with a nonreactive LSI cycle to obtain Si–βSiC ceramics.
2. Three PIP cycles were performed with FUR resin to obtain an optimal degree of densification of the C matrix. Then, HTP was performed to achieve the partial crystallization of the C phase. The final densification was performed with a reactive LSI cycle to obtain RBSiC ceramics.
3. Four PIP cycles were performed with AHPCS to produce a dense SiC matrix. Then, HTP was performed to achieve the crystallization of the SiC into a βSiC. A subsequent infiltration by the FUR resin was performed to obtain free-carbon on the βSiC surface. The final densification was performed with a reactive LSI to obtain RBSiC–βSiC ceramics.
4. Only one PIP was performed with a mixture of AHPCS and graphite powder. Then, HTP was performed to achieve the crystallization of the amorphous SiC phase into βSiC. The final densification was performed with a reactive LSI cycle to obtain RBSiC–βSiC by the reaction between graphite and Si.

Figure 3 schematizes the four cases.

2.4 | Characterization

During the process steps, the mass variation was recorded with a precision balance (0.1 mg resolution) and the sample size was measured using a digital caliper. These operations were performed after PBF, each PIP cycle and after LSI, respectively, to investigate the weight change and the shrinkage of the parts.

Mercury intrusion porosimetry tests (PoreMaster 60, Anton Paar Switzerland AG) were performed in order to evaluate the bulk microporosity, the open pore size distribution, and the pore volume. Analyses were performed by using a pressure range from 0.0014 to 414 MPa.

Helium pycnometry (Ultrapyc3000, Anton Paar QuantaTec Inc.) was used to assess the density of the materials after PBF, PIP, and LSI. Analyses were performed by using a pressure target of 18 psi. A bulk sample piece and sample powder were used for obtaining the apparent and true density values, respectively. Eight tests were performed for each sample.

The phase composition of the ceramic parts after LSI was investigated on crushed sample powder, using an X-ray diffractometer (XRD) (D8 Advance, Bruker Italia Srl) with Cu(k_α) radiation, from 10° to 80°, 0.05°/step, 2 s/step. The Match! Software package (Crystal Impact GbR) was used for a semiautomatic phase identification, supported by data from the PDF-2 database (ICDD-International Centre for Diffraction Data).

Scanning electron microscopy (SEM) analyses (JSM-6010PLUS/LA, Jeol Ltd.) were conducted to investigate the microstructure of the samples after PBF, PIP, and LSI. Surface compositional analysis on selected samples was carried out using energy-dispersive X-ray analysis (EDX). Before the analyses, the samples were fractured and incorporated in a phenolic resin mold.

The mechanical strength of the ceramic samples was evaluated through uniaxial quasi-static compression tests (Zwick Z050, Zwick GmbH & Co.KG). Tests were performed at strain rate of 10^{-3}/s, and a cell load of 50 kN (KAP-S, AST) was used to record the reaction force. The cylindrical sample was placed at the center of the plates and preloaded with a force of 5 N. Ten samples were tested for each type. Before testing, the top and bottom surfaces of the cylinders were machined for flattening.

3 | RESULTS AND DISCUSSION

3.1 | Manufacturing and densification

The two architectures were both successfully 3D printed through the PBF of PA12 powders. The desired geometry of the samples, which consisted of a cylindrical shape with a diameter of 25 ± 0.47 mm and a height of 45 ± 0.64 mm, was successfully produced. The RC lattice consisted of struts with a diameter of 1.1 ± 0.018 mm, whereas the GY structure consisted of surfaces with a thickness of 1.0 ± 0.015 mm (see Section 2.1 for the features of the computational models). The printed parts had a relative strut density of 0.56 ± 0.04, which was measured with

FIGURE 3 Summary of the infiltration strategies for the different cases.

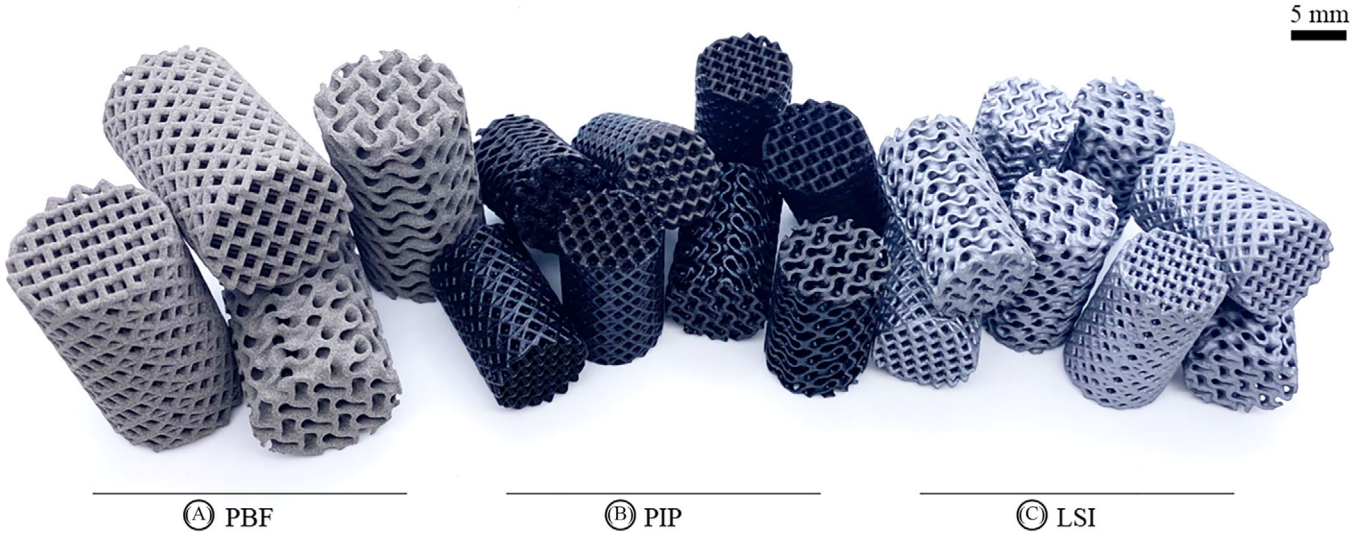

FIGURE 4 Optical imagines of the produced samples after each step of the manufacturing process: (A) polymeric samples after powder bed fusion (PBF); (B) amorphous ceramic samples after polymer infiltration and pyrolysis (PIP); (C) Si-infiltrated ceramic samples after liquid silicon infiltration (LSI).

mercury porosimetry. The optical images of the polymeric samples after the complete AM procedure are shown in Figure 4A.

The parts underwent infiltration and subsequent pyrolysis, resulting in the creation of amorphous ceramics that showed no shape distortion and few macroscopic cracks. As observed in the previous studies,[21,22,40] the conversion process resulted in an isotropic linear shrinkage of approximately 23%.[40] According to the authors' previous work,[22] the decomposition of PA (amide group CO–NH) occurring during the first pyrolysis cycle caused the evolution of CO/CO_2, which introduced some oxygen in the SiC and C

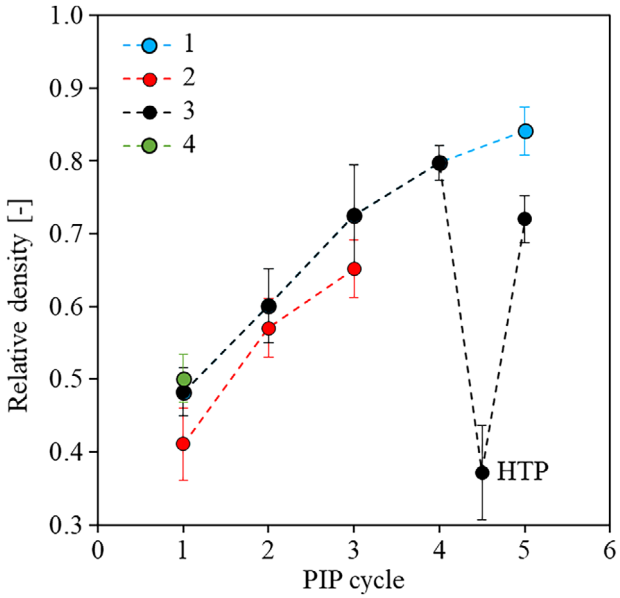

FIGURE 5 Evolution of the relative density (= apparent density/true density) after each polymer infiltration and pyrolysis (PIP) cycle. Case numbering refers to Table 1.

matrices. Cylindrical ceramic structures with a diameter of 19.45 ± 0.25 mm and a height of 34.23 ± 0.15 mm were manufactured in this stage. The diameter of the struts and the thickness of the surfaces also experienced the same shrinkage. In the subsequent PIP cycles, no further shrinkage was observed, and the structures retained their original shape and size (see Figure 4B for optical images of the samples after the final pyrolysis stage). Figure 5 shows the evolution of the relative density after each PIP cycle for the four materials produced. As expected, the results show that after the first conversion, the samples infiltrated with AHPCS produced ceramics with approximately the same relative density and a higher value compared to sample 2, which had been infiltrated with FUR resin. This means that AHPCS has a higher conversion rate than FUR, which is determined by the ceramic yield and the infiltration rate (dependent on the wettability of PA12 with the precursor used). With subsequent infiltrations, the volumetric fraction of the ceramic is increased, thus increasing its relative density. After the fourth infiltration, sample 1 undergoes a final AHPCS infiltration to further increase the relative density, whereas sample 3 undergoes a high-temperature treatment to crystallize SiC and produce additional porosity (resulting in a decrease in relative density). This porosity is then useful for infiltrating it with FUR resin to introduce carbon before LSI. Due to its lower yield, as observed in the initial conversion, the final relative density of sample 3 is lower than that of sample 1. Another reason could be poor wettability or difficulty of the polymer in reaching the free pores inside the material. Table 1 reports the results of the helium pycnometry measurements taken after the final PIP cycle.

Figure 6A,B shows the mercury intrusion porosimetry analysis of the SiC ceramics after 4 PIP cycles at 1000°C (black curves) and the βSiC ceramics after the thermal treatment at 1800°C (red curves). As expected, the high temperature thermal treatment produced a large increase in the microporosity. The large pores in the range of 100–10 μm were present in both microstructures in the same quantity and size. The difference is the generation of smaller pores in the range of 0.3–0.05 μm, due to the crystallization and shrinking of the βSiC phase and to the decomposition of the SiOC phase.[22] The total microporosity of the SiC sample was of 20.2 vol%, and the one of the βSiC samples was of 62.8 vol%. The same increase in the microporosity occurred for the C samples (case #2), due to the formation of CO/CO_2 during the thermal treatment. The obtained increase in the material microporosity was found to be crucial for achieving an efficient subsequent infiltration with molten silicon or with preceramic polymers. Figure 6C shows the two βSiC architectures after the thermal treatment at 1800°C. The pristine shape of the samples was maintained, and a linear shrinkage of 2.5% was observed. Moreover, a light gray/yellow surface color was visible.

The optical images of the silicon infiltrated samples are shown in Figure 4C. A linear shrinkage of about 2%–5% was observed. The samples maintained their pristine shape, and no macrocracks or distortion were observed. However, the RBSiC–βSiC sample of case #4 (see Table 2) showed a dimensional difference with thinner strut and wall of 0.525 ± 0.035 mm, whereas all other materials had struts and surface thicknesses of 0.853 ± 0.089 mm. The difference was due to the different number of PIP cycles performed for the densification of the ceramic matrix before LSI. The #4 ceramics underwent only one PIP cycle, achieving a final relative density of only 0.501. The notable result was the possibility to produce SiC–SiC parts with only one PIP cycle (using a mixture of AHPCS and graphite powder) followed by LSI, maintaining the pristine shape of the lattice (same diameter, height, and topology) but reducing the thickness of the surfaces by about 50%.

Table 2 reports the density measurements taken with the helium pycnometer for the four different materials after LSI.

Figure 7 shows the volume fraction of βSiC, RBSiC, Si, and residual microporosity. The analytic estimation was carried out using Equation (3).

$$\rho_{LSI} = V_{SiC} \cdot \rho_{SiC} + V_{Si} \cdot \rho_{Si} \quad (3)$$

TABLE 1 Helium pycnometry measurements of strut density after the final polymer infiltration and pyrolysis (PIP) cycle.

Case #	Material after the last PIP	Number of PIP cycles	True density (g/cm^3)	Apparent density (g/cm^3)	Final relative density
1	SiC	5	2.403 ± 0.014	2.021 ± 0.088	0.841 ± 0.024
2	C	3	1.921 ± 0.008	1.287 ± 0.071	0.670 ± 0.040
3	C–βSiC	4 + HTP + 1	2.575 ± 0.013	1.854 ± 0.054	0.720 ± 0.032
4	$C_{(g)}$–SiC	1	2.379 ± 0.015	1.192 ± 0.042	0.501 ± 0.028

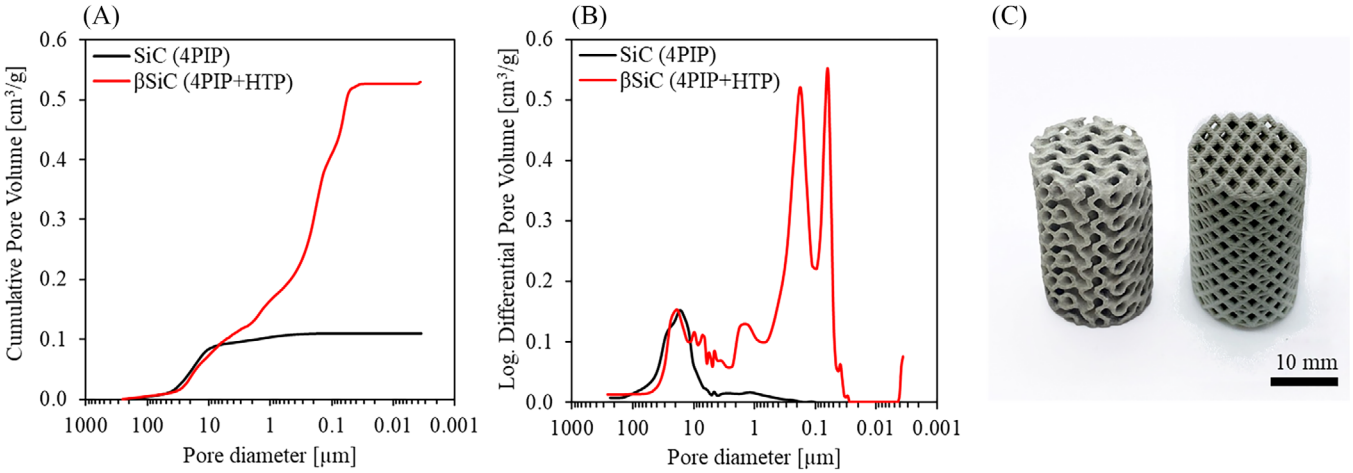

FIGURE 6 Mercury intrusion porosimetry of the SiC ceramics before (black curve, 4 polymer infiltration and pyrolysis [PIP]) and after heating at 1800°C for 1 h (red curve, 4PIP + high temperature pyrolysis [HTP]): (A) Cumulative pore volume and (B) log differential pore volume against the pore diameter; (C) optical image of the βSiC structures after the HTP thermal treatment.

TABLE 2 Helium pycnometry measurements after the liquid silicon infiltration (LSI) process.

Case #	Material after LSI	True density (g/cm^3)	Apparent density (g/cm^3)	Final relative density
1	Si–βSiC	2.845 ± 0.050	2.694 ± 0.112	0.947 ± 0.042
2	RBSiC	3.005 ± 0.031	2.519 ± 0.080	0.838 ± 0.032
3	RBSiC–βSiC	3.173 ± 0.022	2.966 ± 0.047	0.935 ± 0.016
4	RBSiC–βSiC	2.686 ± 0.045	2.571 ± 0.090	0.957 ± 0.035

Abbreviation: RBSiC, reaction bonded SiC.

where ρ_{LSI} is the true density of the material after LSI measured with gas pycnometry (see again Table 2), V_{SiC} and V_{Si} are the volumetric fractions of SiC and Si, respectively, ρ_{SiC} and ρ_{Si} are the theoretical densities of βSiC (3.210 g/cm^3) and Si (2.329 g/cm^3), respectively. The calculation was performed assuming that the density of the residual graphite or carbon (if present) was equal to that of the residual silicon. This means that the Si volume fraction also counts for residual C or graphite in cases 2–4. The reason for this assumption is that the graphite has a density of 2.267 g/cm^3, which is about the same of silicon, and the polymer-derived amorphous carbon had a density of 1.921 g/cm^3 after PIP, and the increase in temperature may have produced an increase in its density. Indeed, literature studies showed that a polycrystalline graphite structure can gradually appear at temperatures above 1500°C.[42–44] Therefore, the density of the residual carbon after LSI can also be assumed similar to the one of silicon.

The higher true density value was obtained by the RBSiC–βSiC of case #3, meaning that the free C reacted very well with Si, producing an additional SiC phase, the RBSiC. The total amount of SiC was estimated to be 90 vol% (36 vol% of βSiC coming from the AHPCS pyrolysis and 54 vol% of RBSiC) with only 3.5 vol% of residual silicon and 6.5 vol% of microporosity. The RBSiC of case #2 produced a high true density despite the fact that its relative density was the lower one. This can be attributed to

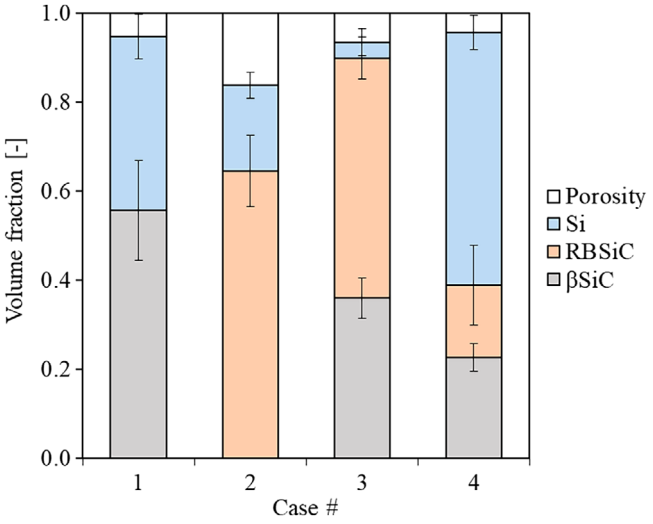

FIGURE 7 Volume fraction estimations on the produced Si-infiltrated ceramic architectures. Case numbering refers to Table 2. The Si volume fraction might include also some residual carbon.

the generation of RBSiC from the reaction of C with Si, which during infiltration produced a clogging of the pore channels and left several pores inside the material (about 16 vol%). However, the SiC content was of 65 vol%, with 19 vol% of residual silicon. The Si–βSiC of case #1 resulted in similar values for the true density, relative density, and volume fractions of the same material of the discs in the previous study,[21] with 56 vol% of βSiC produced by the AHPCS pyrolysis and a high content of residual silicon of 39 vol%. However, the lower true density and higher Si content (57 vol%) were observed in the RBSiC–βSiC sample of case #4. This was due to the low content of SiC derived from only one PIP with AHPCS and to the low amount of graphite added to the infiltrating solution, which did not allow to produce a considerable volume of RBSiC from the reaction with molten Si. However, this ceramic had the higher relative density of 95.7%, probably due to the higher shrinkage of the struts and surfaces. All the materials presented incomplete infiltration, which depended on the pore characteristics, the reactivity of the preform, and capillary blockage. Moreover, it should be noted that the remaining unreacted Si expands during solidification, potentially inducing additional stress concentrations and microcracks.

Table 3 shows the comparison between the density of SiSiC ceramics fabricated by different AM technologies combined with LSI. In general, the true density achieved with the proposed hybrid AM method was in line with the average values found in the literature. A notable result of our work was the very high density values achieved by the sample cases #2 and #3 of 3.005 and 3.173 g/cm^3, respectively. The latter is the highest value found in literature for a SiC ceramics produced via AM followed by LSI. Accordingly, the silicon content of those samples was the lowest. Despite that, the relative density values achieved in our work (see Table 2) were lower than the literature ones, meaning that more PIP cycles are needed to increase the ceramics fraction, and a further optimization of the LSI process is also needed to produce such complex architectures.

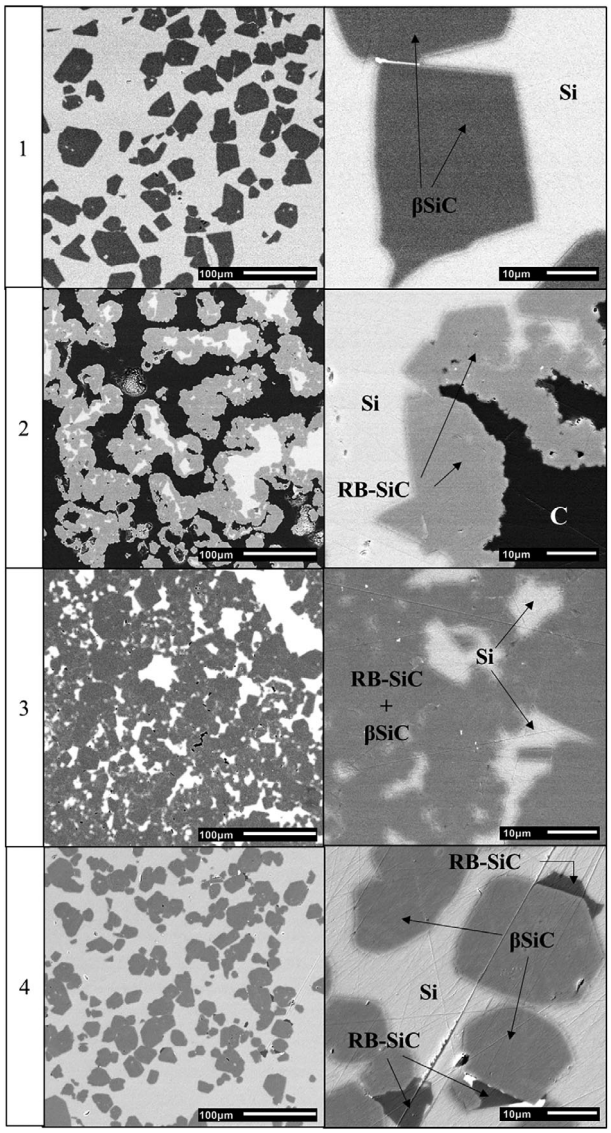

FIGURE 8 Scanning electron microscopy (SEM) micrographs at two magnifications of the ceramic produced with liquid silicon infiltration (LSI). The numbering refers to Table 2.

3.2 | Microstructure

Figure 8 shows the SEM images of the produced Si-infiltrated ceramics taken at different magnifications (the numbering is the same as in Table 2). The sample of

TABLE 3 Comparison between the density of SiSiC ceramics fabricated by different additive manufacturing (AM) technologies combined with liquid silicon infiltration (LSI).

Fabrication method	True density g/cm^3	Relative density	Si content vol%	Reference
PBF + PIP + LSI	2.845	0.947	41	This work
	3.005	0.838	23	
	3.173	0.935	4	
	2.686	0.957	59	
iSLS + LSI	3.06	~1	16.4	17
iSLS + LSI	2.69	–	–	45
iSLS + LSI	2.73	0.990	54	46
iSLS + LSI	2.64	~1	65	47
ROB + LSI	2.94	0.979	22.9	16
BJ + LSI	2.49	0.910	41	12
iSLS + CIP + LSI	2.96	0.940	7	48
LOM + LSI	2.60	–	–	49
BJ + LSI	3.05	~1	15-25	15
SLA + PIP	–	0.848	-	50
SLA + PIP	–	0.935	-	51
SLA + LSI	2.75	–	–	52
SLA + PIP + LSI	2.759	0.977	44	53
SLA + PIP	–	0.826	-	54
SLA + PIP + LSI	–	0.962	-	54
SLA + LSI	2.894	–	–	55
SLA + LSI	2.68	–	–	56

Abbreviations: BJ, binder jetting; CIP, cold isostatic pressure; iSLS, indirect selective laser sintering; LOM, laminated object manufacturing; ROB, robocasting; SLA, stereolithography.

case #1 showed a nearly fully dense material with the presence only of silicon (light gray areas) and beta silicon carbide (dark gray areas), as expected. The volume fractions for βSiC and Si were of 59% and 41%, respectively. The high volumetric presence of Si was due to the nonreactive infiltration, which nevertheless promoted the full crystallization of the amorphous SiC matrix into the βSiC phase; the faceting of the crystals' boundary is also visible.

The sample of case #2 showed the presence of silicon (light gray area) and βSiC (dark gray area). The black area is the resin used to incorporate the material, and an undistinguishable small amount of residual carbon. As expected, the residual silicon was always surrounded by the SiC phase. This demonstrates that, during infiltration, the silicon reacted with the amorphous carbon and produced the RBSiC. The silicon that could not reach the surface of the carbon present within the material became trapped into the formed SiC matrix. Furthermore, 16% of microporosity remained into the material, evidencing an incomplete infiltration. This was due to the clogging of the infiltration channels by the SiC formed on the C surface. In an ideal infiltration, all the silicon should react with all the carbon to form βSiC and leave no residue and no microporosity. The notable result was the possibility to obtain a continuous arrangement of crystals to form a βSiC layered matrix, while in the sample of case #1 the crystals formed individually and separately. The micrographs showed that a large quantity of βSiC was produced during the infiltration, as confirmed by Figure 7.

The sample of case #3 showed an intermediate microstructure with respect to the previous ones. In this case, a large amount of βSiC is visible (dark gray areas) with respect to the silicon phase (light gray areas). Two βSiC phases were formed: one derived from the crystallization of the preceramic polymer, and another derived from the reaction between the carbon and the silicon during infiltration RBSiC. These two phases were not distinguishable with SEM. However, the outstanding result was the production of a nearly fully dense part, with 96 vol% of βSiC and only 4 vol% of residual silicon.

The sample of case #4 showed the presence of three phases: A high amount of residual silicon (light gray areas),

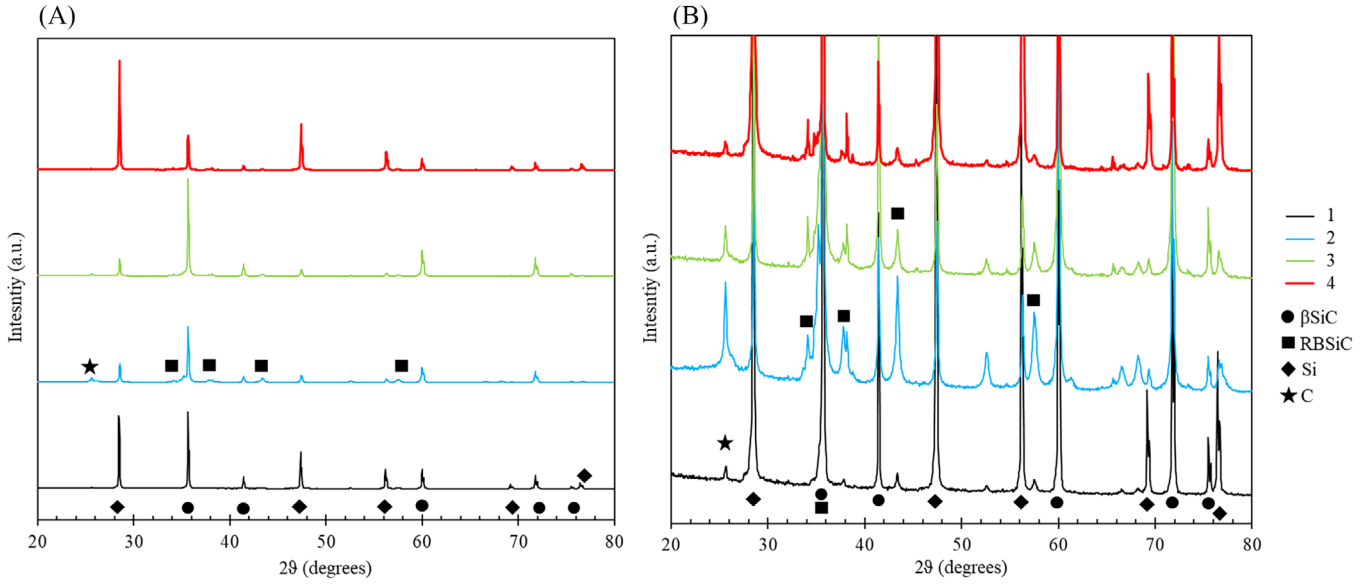

FIGURE 9 X-ray diffractometer (XRD) analysis of the Si-infiltrated ceramic architectures: (A) full chart and (B) higher magnification. The numbers refer to the cases in Table 2.

the βSiC (dark gray areas) derived from the precursor, and the RBSiC (black areas) derived by the reaction between the silicon and the graphite powder. In this case, the high quantity of residual silicon (59 vol%) was justified by only one PIP cycle having being performed for this material. The sample before LSI had a microporosity of about 50 vol%. After LSI the microporosity was only 4 vol%, so the lowest obtained between the four cases. The βSiC formed by the AHPCS conversion was clearly visible in higher quantity (24 vol%) with respect to the RBSiC (17 vol%), which was probably masked by the large amount of silicon present. No significant differences in terms of composition were observed between the two types of produced SiC, as assessed by EDX analysis.

3.3 | Phase composition

Figure 9 reports the results of the XRD analyses. The phase composition of the sample of case #1 (black curve) showed the presence of fully crystallized βSiC and of a large quantity of Si, besides a limited amount of graphitic carbon. Amorphous SiC appears to have been completely eliminated from the sample after Si infiltration. The phase composition of the sample of case #2 (blue curve) was comprised by a lower amount of Si, much more graphitic carbon, and βSiC. However, there was a notable difference between the βSiC derived from the crystallization of AHPCS and the one generated by the reaction between amorphous carbon and silicon RBSiC. In particular, two additional peaks located at ~34° and 38° could be observed, which can be attributed to stacking faults[57,58] in the crystals (these peaks are typical for α-SiC, but the formation temperature of this phase is higher than 2000°C). As expected, the phase composition of the sample of case #3 (green curve) was comprised by a very low amount of Si, a limited amount of graphitic carbon, and βSiC. The good crystallization of βSiC and its large volume fraction is visible. The phase composition of the sample of case #4 (red curve) comprised βSiC, a limited amount of graphitic carbon, and a large amount of Si.

3.4 | Mechanical properties

Figure 10 shows the compressive strength of the tested ceramics after LSI as a function of the true density of the samples, measured with helium pycnometry. No significant differences were observed when testing the different materials despite the infiltration methods being different, and in all cases a brittle fracture occurred followed by the propagation of microcracks in the cells of the structure. The large error bars can be attributed to the uneven bottom and top surfaces of the specimen, despite attempts made to level them. It is clear that the cellular morphology has a marked influence on mechanical performance, because the two architectures have the same geometric macroporosity (see again Section 2.1). The strength of the GY structures was double than that of the RCs lattices. Therefore, the morphology plays a critical role in determining the mechanical properties. In general, superior stiffness is achieved by cellular structures with features orientated along the loading direction (such as GY surfaces) which outperform the others (RC struts). As expected, the

TABLE 4 Comparison of the compression strength, density, and macroporosity between the produced SiSiC ceramics and other SiSiC lattices produced with other additive manufacturing (AM) methods from the literature[46,59]

Fabrication method	Material	Architecture	Sample size mm^3	Macro porosity %	True density g/cm^3	Apprent density g/cm^3	Relative density	Si content content vol%	Strength MPa	Reference
PBF + PIP + LSI	Si–βSiC	RC	D19H33	67	2.845	2.694	0.947	41 ± 9	9.2 ± 0.4	This study
	RBSiC	RC	D19H33	67	3.005	2.519	0.838	23 ± 3	10.1 ± 2.2	
	RBSiC–βSiC	RC	D19H33	67	3.173	2.966	0.935	4 ± 3	11.8 ± 3.0	
	RBSiC–βSiC	RC	D19H33	67	2.686	2.571	0.957	59 ± 4	3.2 ± 0.5	
	Si–βSiC	GY	D19H33	67	2.845	2.694	0.947	41 ± 9	14.9 ± 3.1	
	RBSiC	GY	D19H33	67	3.005	2.519	0.838	23 ± 3	23.5 ± 4.8	
	RBSiC–βSiC	GY	D19H33	67	3.173	2.966	0.935	4 ± 3	24.7 ± 2.2	
	RBSiC–βSiC	GY	D19H33	67	2.686	2.571	0.957	59 ± 4	10.7 ± 1.9	
iSLS + PIP + LSI	SiSiC	GY-strut	20 × 20 × 20	75	2.711	2.698	0.995	56	2.304	46
	SiSiC	GY-strut	20 × 20 × 20	70	2.735	2.719	0.994	53	3.542	
	SiSiC	GY-strut	20 × 20 × 20	65	2.764	2.747	0.994	50	4.689	
	SiSiC	GY-strut	20 × 20 × 20	60	2.699	2.687	0.996	58	7.821	
	SiSiC	GY-strut	20 × 20 × 20	55	2.732	2.714	0.993	54	10.037	
	SiSiC	GY-strut	20 × 20 × 20	50	2.757	2.74	0.994	51	11.104	
	SiSiC	GY-strut	20 × 20 × 20	45	2.747	2.739	0.997	52	16.267	
Replica	SiSiC	Random	35 × 35 × 35	80	2.765	–	–	50	2	59
	SiSiC	RC	35 × 35 × 35	85	2.765	–	–	50	1	
	SiSiC	Cube	35 × 35 × 35	85	2.765	–	–	50	6.5	
	SiSiC	Kelvin	35 × 35 × 35	85	2.765	–	–	50	6	
	SiSiC	Octet	35 × 35 × 35	80	2.765	–	–	50	5	

Abbreviations: GY, gyroid; iSLS, indirect selective laser sintering; LSI, liquid silicon infiltration; PBF, powder bed fusion; PIP, polymer infiltration and pyrolysis; RBSiC, reaction bonded SiC; RC, rotated cube.

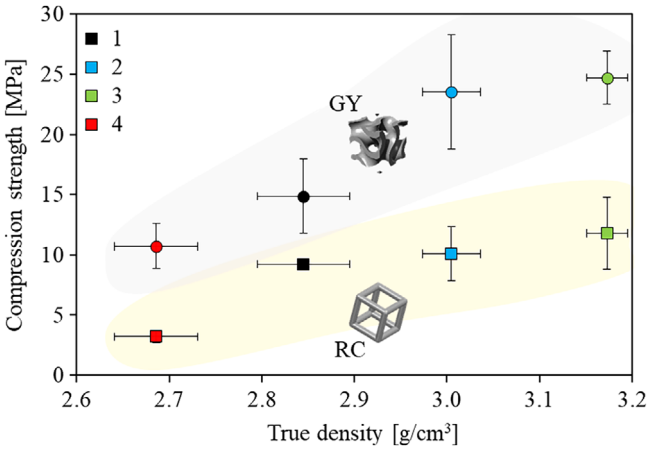

FIGURE 10 Mechanical tests result of the ceramics produced with liquid silicon infiltration (LSI): compression strength against true density. The numbering refers to Table 2.

overall mechanical properties increase with increasing of the true density, since adding more SiC phase is contributing to the stiffening and strengthening of the material. The influence of residual microporosity on mechanical performance appears to be insignificant. Samples #1 and #4 possessed lower microporosity compared to samples #2 and #3. Notably, sample #2 possessed a volume of microporosity three times higher than the others, yet had significantly superior mechanical strength. This observation suggests the potential for further improvement in mechanical performance if the samples achieve full density. The compression strength of the GY samples was found to be superior to that reported in the literature for cellular SiSiC ceramics obtained by the replica method, which had a strength ranging from 1 to 16.3 MPa at a true density of 2.765 g/cm^3, a relative density of 0.99, and a geometric macroporosity ranging from 45 to 80 vol%.[46,59]

Table 4 shows the comparison of the compression strength, density, and macroporosity between the produced SiSiC ceramics and other SiSiC lattices produced with other AM methods from the literature.[46,59] The produced ceramic architectures had superior compressive strength (more than double) with respect to ceramic structures of the same materials found in literature. Moreover, the density achieved by the RBSiC–βSiC ceramics is much higher.

4 | CONCLUSIONS

In this study, the utilization of the previous developed hybrid AM process proved to be a successful method for producing intricate SiC-based ceramic architectures by reactive infiltration. By employing PBF of PA12 powders, two complex structures were designed and 3D printed. Subsequently, these porous preforms underwent a series of PIP cycles to convert them into ceramics. It was observed that a small amount of oxygen derived from PA12 was present in all compositions. Despite a substantial linear shrinkage of 23% during the initial conversion process, the parts maintained their original shape without any macrocracks or distortions. The final stage of densification involved LSI of four distinct ceramic matrices: SiC ceramics, C ceramics, C–βSiC ceramics, and graphite–SiC ceramics. During LSI, the ceramic phase crystallized, facilitating complete infiltration by molten silicon and resulting in the production of the final Si–βSiC, RBSiC, and RBSiC–βSiC ceramics. Notably, the RBSiC–βSiC samples (case #3) had a microstructure comprised of crystalline βSiC, reaction-bonded βSiC, and residual Si with volume fractions of 36%, 54%, and 3.5%, respectively, with only 6.5 vol% of residual microporosity. The GY samples exhibited a compressive strength of 24.7 MPa, which is much higher than that of other SiSiC cellular ceramics found in the literature. These findings demonstrate the potential of the novel developed approach and highlight the successful fabrication of complex ceramic structures with desirable properties. This manufacturing approach also allowed to produce complex structures with wall thickness <0.5 mm, which cannot be achieved with other AM techniques on the market (binder jetting and direct ink writing above all).

ACKNOWLEDGMENTS

The authors have nothing to report.

CONFLICT OF INTEREST STATEMENT

The authors declare no conflicts of interest for this work.

ORCID

Marco Pelanconi https://orcid.org/0000-0002-0354-4893
Samuele Bottacin https://orcid.org/0009-0006-4241-8546
Giovanni Bianchi https://orcid.org/0000-0002-1685-5420
Dietmar Koch https://orcid.org/0000-0003-4504-8721
Paolo Colombo https://orcid.org/0000-0001-8005-6618
Alberto Ortona https://orcid.org/0000-0002-1764-5871

REFERENCES

1. Gibson I. Additive manufacturing technologies 3D printing, rapid prototyping, and direct digital manufacturing. Berlin: Springer; 2015.
2. Pelanconi M, Rezaei E, Ortona A. Cellular ceramic architectures produced by hybrid additive manufacturing: a review on the evolution of their design. J Ceram Soc Jpn. 2020;128:595–604.
3. Pelanconi M, Ortona A. Review on the design approaches of cellular architectures produced by additive manufacturing. In:

Meboldt M, Klahn C, editors. Industrializing additive manufacturing. Berlin: Springer International Publishing; 2021. p. 52–64.
4. Gómez-Gómez A, Moyano JJ, Román-Manso B, Belmonte M, Miranzo P, Osendi MI. Highly-porous hierarchical SiC structures obtained by filament printing and partial sintering. J Eur Ceram Soc. 2019;39:688–95.
5. Du W, Singh M, Singh D. Binder jetting additive manufacturing of silicon carbide ceramics: development of bimodal powder feedstocks by modeling and experimental methods. Ceram Int. 2020;46:19701–7.
6. Liu R, Chen G, Qiu Y, Chen P, Shi Y, Yan C, et al. Fabrication of porous SiC by direct selective laser sintering effect of boron carbide. Metals (Basel). 2021;11:737.
7. Li Q, Dong S, Wang Z, Shi G. Fabrication and properties of 3-D Cf/ZrB2–ZrC–SiC composites via polymer infiltration and pyrolysis. Ceram Int. 2013;39:5937–41.
8. Xiong H, Zhao L, Chen H, Luo H, Yuan X, Zhou K, et al. Building SiC-based composites from polycarbosilane-derived 3D–SiC scaffolds via polymer impregnation and pyrolysis (PIP). J Eur Ceram Soc. 2021;41:1121–31.
9. Sergi D, Camarano A, Molina JM, Ortona A, Narciso J. Surface growth for molten silicon infiltration into carbon millimeter-sized channels: Lattice–Boltzmann simulations, experiments and models. Int J Mod Phys C. 2015;27:1650062.
10. Bougiouri V, Voytovych R, Rojo-Calderon N, Narciso J, Eustathopoulos N. The role of the chemical reaction in the infiltration of porous carbon by NiSi alloys. Scr Mater. 2006;54:1875–78.
11. Terrani K, Jolly B, Trammell M. 3D printing of high-purity silicon carbide. J Am Ceram Soc. 2020;103:1575–81.
12. Cramer CL, Elliott AM, Lara-Curzio E, Flores-Betancourt A, Lance MJ, Han L, et al. Properties of SiC–Si made via binder jet 3D printing of SiC powder, carbon addition, and silicon melt infiltration. J Am Ceram Soc. 2021;104:5467–78.
13. Cramer CL, Armstrong H, Flores-Betancourt A, Han L, Elliot AM, Lara-Curzio E, et al. Processing and properties of SiC composites made via binder jet 3D printing and infiltration and pyrolysis of preceramic polymer. Int J Ceram Eng Sci. 2020;2:320–31.
14. Polozov I, Razumov N, Masaylo D, Silin A, Lebedeva Y, Popovich A. Fabrication of silicon carbide fiber-reinforced silicon carbide matrix composites using binder jetting additive manufacturing from irregularly-shaped and spherical powders. Materials. 2020;13:1766.
15. Zocca A, Lima P, Diener S, Katsikis N, Günster J. Additive manufacturing of SiSiC by layerwise slurry deposition and binder jetting (LSD-print). J Eur Ceram Soc. 2019;39:3527–33.
16. Wahl L, Lorenz M, Biggemann J, Travitzky N. Robocasting of reaction bonded silicon carbide structures. J Eur Ceram Soc. 2019;39:4520–26.
17. Meyers S, De Leersnijder L, Vleugels J, Kruth J-P. Direct laser sintering of reaction bonded silicon carbide with low residual silicon content. J Eur Ceram Soc. 2018;38:3709–17.
18. Colombo P. Polymer derived ceramics: from nano-structure to applications. Lancaster: DEStech Publications, Inc; 2010.
19. Grossin D, Montón A, Navarrete-Segado P, Özmen E, Urruth G, Maury F, et al. A review of additive manufacturing of ceramics by powder bed selective laser processing (sintering /melting): calcium phosphate, silicon carbide, zirconia, alumina, and their composites. Open Ceram. 2021;5:100073
20. He R, Zhou N, Zhang K, Zhang X, Zhang L, Wang W, et al. Progress and challenges towards additive manufacturing of SiC ceramic. J Adv Ceram. 2021;10:637–74.
21. Pelanconi M, Bianchi G, Colombo P, Ortona A. Fabrication of dense SiSiC ceramics by a hybrid additive manufacturing process. J Am Ceram Soc. 2022;105:786–93.
22. Pelanconi M, Colombo P, Ortona A. Additive manufacturing of silicon carbide by selective laser sintering of PA12 powders and polymer infiltration and pyrolysis. J Eur Ceram Soc. 2021;41:5056–65.
23. Macdonald L. Facile fabrication of SiC matrix composites using novel preceramic polymers. Adv SiC/SiC Ceram Compos: Dev Appl Energy Syst. 2006;144:87–95. https://doi.org/10.1002/9781118406014.ch7
24. Dong SM, Katoh Y, Kohyama A, Schwab ST, Snead LL. Microstructural evolution and mechanical performances of SiC/SiC composites by polymer impregnation/microwave pyrolysis (PIMP) process. Ceram Int. 2002;28:899–905.
25. Kotani M, Kohyama A, Okamura K, Inoue T. Fabrication of high performance SiC/SiC composite by polymer impregnation and pyrolysis method. *23rd Annual Conference on Composites, Advanced Ceramics, Materials, and Structures: B: Ceramic Engineering and Science Proceedings*. 1999;20:309–16. https://doi.org/10.1002/9780470294574.ch36
26. Sreeja R, Swaminathan B, Painuly A, Sebastian TV, Packirisamy S. Allylhydridopolycarbosilane (AHPCS) as matrix resin for C/SiC ceramic matrix composites. Mater Sci Eng B Solid State Mater Adv Technol. 2010;168:204–7.
27. Kopeliovich D. Advances in manufacture of ceramic matrix composites by infiltration techniques. Woodhead Publishing Series in Composites Science and Engineering. In: Advances in Ceramic Matrix Composites. 2nd ed. Woodhead Publishing; 2018. p. 93–119.
28. Kopeliovich D. Advances in the manufacture of ceramic matrix composites using infiltration techniques. In: Advances in ceramic matrix composites. Amsterdam: Elsevier; 2014. p. 79–108.
29. Zhang H, Yang Y, Liu B, Huang Z. The preparation of SiC-based ceramics by one novel strategy combined 3D printing technology and liquid silicon infiltration process. Ceram Int. 2019;45:10800–10804.
30. Sangsuwan P, Orejas JA, Gatica JE, Tewari SN, Singh M. Reaction-bonded silicon carbide by reactive infiltration. Ind Eng Chem Res. 2001;40:5191–98.
31. Qian J-M, Wang J-P, Jin Z-H. Preparation and properties of porous microcellular SiC ceramics by reactive infiltration of Si vapor into carbonized basswood. Mater Chem Phys. 2003;82:648–53.
32. Wang Y, Tan S, Jiang D. The effect of porous carbon preform and the infiltration process on the properties of reaction-formed SiC. Carbon. 2004;42:1833–39.
33. Qian J-M, Jin Z-H, Wang X-W. Porous SiC ceramics fabricated by reactive infiltration of gaseous silicon into charcoal. Ceram Int. 2004;30:947–51.
34. Koyanagi T, Terrani K, Harrison S, Liu J, Katoh Y. Additive manufacturing of silicon carbide for nuclear applications. J Nucl Mater. 2021;543:152577.

35. Bhatia A, Sehgal AK. Additive manufacturing materials, methods and applications: a review. Mater Today Proc. 2023;81:1060–67.
36. Kulkarni SR, Velisoju VK, Tavares F, Dikhtiarenko A, Gascon J, Castaño P. Silicon carbide in catalysis: from inert bed filler to catalytic support and multifunctional material. Catal Rev Sci Eng. 2023;65:174–237.
37. Barbato M, Zavattoni S, Vignoles GL, Ortona A. Thermal design, optimization and additive manufacturing of ceramic regular structures to maximize the radiative heat transfer. Mater Des. 2019;163:107539.
38. She X, Huang AQ, Lucia O, Ozpineci B. Review of silicon carbide power devices and their applications. IEEE Trans Ind Electron. 2017;64:8193–205.
39. Saddow SE, Agarwal AK. Advances in silicon carbide processing and applications. Boston: Artech House; 2004.
40. Pelanconi M, Bottacin S, Colombo P, Ortona A. Powder bed fusion of polyamide powders combined with different preceramic polymers infiltration and pyrolysis to produce complex-shaped ceramics. J Eur Ceram Soc. 2023;43:5871–81. https://doi.org/10.1016/j.jeurceramsoc.2023.06.053
41. Pampuch R, Walasek E, Bialoskórski J. Reaction mechanism in carbon-liquid silicon systems at elevated temperatures. Ceram Int. 1986;12:99–106.
42. Eom Y, Son SM, Kim YE, Lee J-E, Hwang S-H, Chae HG. Structure evolution mechanism of highly ordered graphite during carbonization of cellulose nanocrystals. Carbon. 2019;150:142–52.
43. Sagues WJ, Jain A, Brown D, Aggarwal S, Suarez A, Kollman M, et al. Are lignin-derived carbon fibers graphitic enough? Green Chem. 2019;21:4253–65.
44. Köhnke J, Rennhofer H, Lichtenegger H, Mahendran AR, Unterweger C, Prats-Mateu B, et al. Electrically conducting carbon microparticles by direct carbonization of spent wood pulping liquor. ACS Sustainable Chem Eng. 2018;6:3385–91.
45. Song S, Gao Z, Lu B, Bao C, Zheng B, Wang L. Performance optimization of complicated structural SiC/Si composite ceramics prepared by selective laser sintering. Ceram Int. 2020;46:568–75.
46. Wu S, Yang L, Wang C, Yan C, Shi Y. Si/SiC ceramic lattices with a triply periodic minimal surface structure prepared by laser powder bed fusion. Addit Manuf. 2022;56:102910.
47. Friedel T, Travitzky N, Niebling F, Scheffler M, Greil P. Fabrication of polymer derived ceramic parts by selective laser curing. J Eur Ceram Soc. 2005;25:193–97.
48. Liu K, Wu T, Bourell DL, Tan Y, Wang J, He M, et al. Laser additive manufacturing and homogeneous densification of complicated shape SiC ceramic parts. Ceram Int. 2018;44:21067–75.
49. Windsheimer H, Travitzky N, Hofenauer A, Greil P. Laminated object manufacturing of preceramic-paper-derived Si–SiC composites. Adv Mater. 2007;19:4515–19.
50. He R, Ding G, Zhang K, Li Y, Fang D. Fabrication of SiC ceramic architectures using stereolithography combined with precursor infiltration and pyrolysis. Ceram Int. 2019;45:14006–14.
51. Ding G, He R, Zhang K, Zhou N, Xu H. Stereolithography 3D printing of SiC ceramic with potential for lightweight optical mirror. Ceram Int. 2020;46:18785–90.
52. Zhang H, Yang Y, Hu K, Liu B, Liu M, Huang Z. Stereolithography-based additive manufacturing of lightweight and high-strength Cf/SiC ceramics. Addit Manuf. 2020;34:101199.
53. Chang H, Tang J, Guo X, Zhu Y, Liu M, Wei Y, et al. Stereolithography-based additive manufacturing of RB–SiC ceramics by a two-step sintering method. Ceram Int. 2023;49:1085–91.
54. Bai X, Ding G, Zhang K, Wang W, Zhou N, Fang D, et al. Stereolithography additive manufacturing and sintering approaches of SiC ceramics. Open Ceram. 2021;5:100046.
55. Li W, Cui C, Bao J, Zhang G, Li S, Wang G. Properties regulation of SiC ceramics prepared via stereolithography combined with reactive melt infiltration techniques. Ceram Int. 2021;47:33997–4004.
56. Tang J, Chang H, Guo X, Liu M, Wei Y, Huang Z, et al. Preparation of carbon fiber-reinforced SiC ceramics by stereolithography and secondary silicon infiltration. Ceram Int. 2022;48:25159–67.
57. Danko GA, Silberglitt R, Colombo P, Pippel E, Woltersdorf J. Comparison of microwave hybrid and conventional heating of preceramic polymers to form silicon carbide and silicon oxycarbide ceramics. J Am Ceram Soc. 2000;83:1617–25.
58. Niu F-X, Wang Y-X, Fu S-L, Ma L-R, Wang C-G. Ferrocene-assisted growth of SiC whiskers with hexagonal cross-section from a preceramic polymer. Ceram Int. 2017;43:12983–87.
59. Rezaei E, Haussener S, Gianella S, Ortona A. Early-stage oxidation behavior at high temperatures of SiSiC cellular architectures in a porous burner. Ceram Int. 2016;42:16255–61.

SUPPORTING INFORMATION

Additional supporting information can be found online in the Supporting Information section at the end of this article.

How to cite this article: Pelanconi M, Bottacin S, Bianchi G, Koch D, Colombo P, Ortona A. High-strength Si–SiC lattices prepared by powder bed fusion, infiltration-pyrolysis, and reactive silicon infiltration. J Am Ceram Soc. 2024;1–15. https://doi.org/10.1111/jace.19750